JOURNAL OF PROPULSION AND POWER
Vol. 34, No. 6, November–December 2018

Linear Acoustic Analysis of Main Combustion Chamber of an Oxidizer-Rich Staged Combustion Engine

Christopher Lioi,* David Ku,† and Vigor Yang‡
Georgia Institute of Technology, Atlanta, Georgia 30327-0150

DOI: 10.2514/1.B36878

A comprehensive linear acoustic analysis of the main combustion chamber of an oxidizer-rich staged combustion engine is presented. The theoretical basis is an acoustic wave equation derived from the conservation equations that characterize unsteady flow motions in the chamber. The physical model mimics the RD-170 main combustion chamber and includes all the geometric details, including the upstream flow distributor, oxidizer plenum, injector assembly, and main chamber. Damping effects associated with the flow distributor plate and injectors are accounted for by means of impedance boundary conditions. Acoustic communication between the main chamber and oxidizer manifold via the injector assembly is found to be significant. Acoustic waves excited in the main chamber propagate upstream and interact with the oxidizer dome, where they are partially damped by the flow distributor. The influence of baffle injectors on the chamber acoustic behavior is also studied. It is found that the largest contributor to damping is increased transport of acoustic energy out of the domain due to advective mean flow effects.

Nomenclature

c = speed of sound
$\mathcal{D}$ = acoustic dipole sources
$\mathcal{F}$ = fluctuating interphase momentum transfer, due to phase change and drag forces
k = wave number, $\Omega/\bar{c}$
$\mathcal{M}$ = acoustic monopole sources
$\boldsymbol{n}$ = inner unit normal vector of chamber wall
$\mathcal{P}$ = fluctuating energy release due to combustion, work done by condensed phase, energy transfer due to phase change
p = pressure
$\mathcal{T}$ = acoustic transmission coefficient
$\mathcal{R}$ = acoustic reflection coefficient
Re = Reynolds number
St_ω = Strouhal number
$\boldsymbol{u}$ = velocity vector
u_c = bias flow velocity
Z = acoustic impedance, $p'/(\boldsymbol{u}'\cdot\boldsymbol{n})$
γ = ratio of specific heats
$\psi(\boldsymbol{x})$ = mode shape of chamber normal mode
$\eta(t)$ = time-dependent amplitude of chamber normal mode
Ω = complex eigenfrequency, $\omega + i\alpha$ ($\omega =$ angular frequency of oscillation, $\alpha =$ growth rate)
θ = angle between incident wave and boundary surface
χ = Rayleigh conductivity of flow distributor orifice, $2R(\gamma - i\delta)$ ($\gamma =$ resistive component, $\delta =$ reactive component, $R =$ orifice radius)

Superscripts

$-$ = averaged quantity
$'$ = fluctuating quantity
$\hat{}$ = complex amplitude

I. Introduction

THE development and operation of propulsion engines are hindered by the occurrence of combustion instabilities. These large-amplitude self-excited acoustic oscillations have negative effects on engine performance and lifetime, and in extreme cases may cause catastrophic failure. A considerable body of research has emerged that treats instability problems in devices such as gas turbines [1], ramjets and scramjets [1], ramjets and scramjets [2–5], solid propellant rocket motors [6,7], and liquid-fueled rocket engines [8,9]. Nonetheless, accurate and consistent a priori prediction of the occurrence of combustion instabilities remains a difficult task. The purpose of this paper is to develop an integrated analytical/numerical modeling framework for acoustic instabilities in the main combustion chamber of an oxidizer-rich staged combustion (ORSC) engine. Such engines have recently received much attention for use in heavy-lift launch vehicles [10]. The present work represents the first attempt to conduct a comprehensive analysis of the entire combustion chamber, including all geometric details.

Liquid rocket engines may broadly be categorized according to the thermodynamic cycle they employ to drive their propellant turbopump assembly [11]. Three common types of engine cycles are expander, gas generator, and staged combustion. In an expander cycle, no combustion takes place before the propellants enter the thrust chamber. The fuel is heated and expands as it is circulated around the outside of the thrust chamber. In a gas generator cycle, a fraction of the propellants is burned before entering the main combustion chamber and used to drive the turbopump before being exhausted into the diverging portion of the exit nozzle. This allows for higher pressure head to drive the pump system relative to the expander cycle. In a staged combustion cycle, a larger fraction of the propellants is combusted in one or more preburners before being passed through the turbine. This may be done in either fuel- or oxidizer-rich mode. The turbine exhaust is then delivered to the main combustion chamber, where it is burned with the portion of the propellants that bypassed the preburner. Staged combustion engines possess numerous advantages over designs employing the other two cycles, in particular lower gas temperatures entering the turbine, and higher chamber pressures. High pressures generally have the effect of increasing the overall efficiency and specific thrust of the engine. Furthermore, ORSC engines exhibit little to no coking or soot formation. However, staged combustion engines are typically heavier and more complex than their gas generator and expander cycle counterparts. The added complexity coupled with high pressure make designing staged combustion engines more challenging than designing engines using the other cycles. The Russian RD-170, shown schematically in Fig. 1, is a well-known example of an ORSC engine [10–13], and is used throughout the present work as a case study.

Received 18 August 2017; revision received 8 May 2018; accepted for publication 9 May 2018; published online 30 July 2018. Copyright © 2018 by Christopher B. Lioi, David D. Ku, and Vigor Yang. Published by the American Institute of Aeronautics and Astronautics, Inc., with permission. All requests for copying and permission to reprint should be submitted to CCC at www.copyright.com; employ the ISSN 0748-4658 (print) or 1533-3876 (online) to initiate your request. See also AIAA Rights and Permissions www.aiaa.org/randp.

*Graduate Research Assistant, Aerospace Engineering; clioi3@gatech.edu. Student Member AIAA.

†Research Engineer, School of Aerospace Engineering; currently Research Engineer, Aerojet Rocketdyne; d.ku@gatech.edu. Member AIAA.

‡William R. T. Oakes Professor and Chair, School of Aerospace Engineering; vigor.yang@aerospace.gatech.edu. Fellow AIAA.

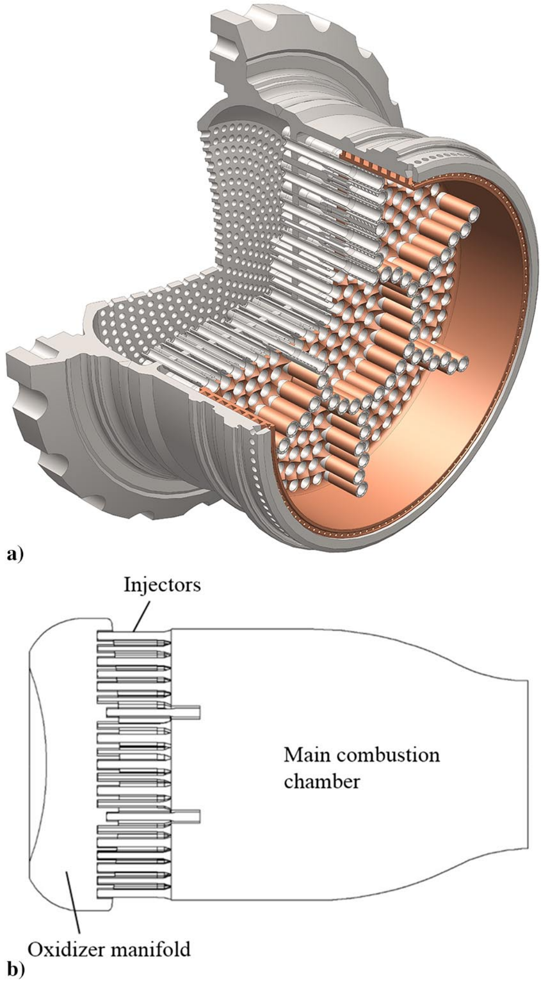

Fig. 1 a) Main combustion chamber of ORSC engine. b) Longitudinal cutaway of chamber. Adapted from Yang et al. [10].

Combustion instabilities result from a resonant coupling between heat release and flow motions within a chamber. In a real combustion device, low-amplitude intrinsic fluctuations exist in the form of turbulence and broadband acoustic noise. As the flame is perturbed by these fluctuations, the heat release rate is modulated. According to Rayleigh's criterion [14], if the relative phase between the unsteady heat release rate and the acoustic pressure is within 90 deg, then energy will be transferred to the acoustic field. If more energy is added than is radiated away or dissipated internally, the acoustic waves will grow until eventually limited by nonlinear processes. At this point, the system is said to have attained a limit cycle. The final state typically consists of large-amplitude acoustic oscillations concentrated in narrow bands about one or more of the natural frequencies of the chamber.

Nonlinear processes also play a role in a type of behavior known as triggered instability [15–18]. In this case, the system is stable with respect to all perturbations below some threshold amplitude. Pulses above this amplitude may cause the system to transition to a limit cycle. Another related effect arises from the non-normality of the differential equations governing the unsteady flow quantities. Even when the system possesses no unstable eigenvalues, transient growth of infinitesimal pressure disturbances may occur [17,18]. If the amplitude of these oscillations grows large enough that nonlinear effects become important, the system may be triggered. It is thus conceivable that even a completely linearly stable system may spontaneously transition to a limit cycle. Determination of nonlinear stability behavior is a considerable challenge and will be treated in future work. The present paper focuses on linear acoustic analysis, which is a fundamental problem and forms the basis of many nonlinear formulations [15,16,19,20].

Strategies for predicting combustion instabilities vary on a continuum from purely analytical to purely numerical. Several linear stability analyses have been developed, such as the now classic formulations of Crocco and Cheng [21] and those collected in the volume by Harrje and Reardon [22], as well as the more modern Galerkin projection method of Zinn and Powell [23] as well as that of Culick and collaborators [24,25]. In the latter framework, the unsteady pressure and velocity fields are approximated as a Fourier synthesis of the chamber normal modes $\psi(x)$, weighted with time-varying coefficients $\eta_n(t)$. A spatial averaging procedure is applied to extract a set of coupled ordinary differential equations governing the time evolution of the modal amplitudes $\eta_n(t)$. Ultimately, an expression for the complex growth constant associated with each physical process can be derived in the form of surface or volume integrals of the unperturbed chamber modes. While physically illuminating, the necessary integrals arising in the scheme can be evaluated exactly only for simple canonical geometries and flowfields. On the other end of the modeling spectrum is a purely numerical treatment. The complete set of governing equations is solved over the domain, thus automatically accounting for all possible physics with minimal modeling. This remains an extremely computationally expensive task, to the extent that it may not be practical to run a sufficient number of cases during the design stage of an engine. A general strategy that has emerged as an optimum solution between these two extremes is to numerically compute the acoustic field within a chamber by solving linearized perturbation equations, with all processes affecting acoustic damping or driving being modeled either by theories or more detailed computations. Several methods are available in the literature, including formulations based on linearized Euler equations [26], acoustic perturbation equations [27], and the Helmholtz equation [28–30].

In the present work a numerical eigenvalue analysis is conducted directly on the general acoustic wave equation, incorporating all geometrical details, and source terms arising from volumetric and boundary effects. The commercial finite-element code COMSOL is employed to carry out the calculations. Similar approaches have recently been adopted by several researchers [29,30], but with varying levels of approximation. Further, only limited physics are incorporated.

Almost all previous analyses of liquid rocket combustion stability consider a domain consisting only of the main chamber downstream of the injector face plate. Ad-hoc assumptions are made for upstream boundary conditions. For example, Pieringer et al. [27] assume that the fluctuating mass flow rate vanishes at the injection plane. This is equivalent to specifying a choked flow, a questionable assumption for most liquid rocket engine injectors. Schulze and Sattelmayer [31] correctly note that coupling with feed system components, such as the injectors and propellant manifolds, may introduce significant additional damping and/or driving effects and must be incorporated in a more comprehensive manner. However, they account for the coupling by means of a scattering matrix, which is assumed to be identical for all injectors. In the present work, no such assumption is made because the entire gas volume consisting of the main chamber, injectors, and oxidizing gas manifold is included in the domain of a single eigenvalue analysis. The approach also eliminates the need for separate determination of scattering matrices from either theory or computations.

Figure 1 shows a schematic of the main combustion chamber of an ORSC engine using oxygen and kerosene as propellants similar to the well-studied RD-170 engine [10–13]. As shown, oxidizer is introduced through the upstream flow distributor, whereas fuel is introduced separately into the injector manifold. Two types of injector elements are used, respectively, referred to as main and baffle elements. Baffle elements are so called because they are offset axially from the main injector elements so as to form baffle compartments. The cutaway view in Fig. 2 shows the differences in configuration between the two element types.

Baffles have proven to be an effective passive method for stabilizing acoustic motions in combustion chambers [32–34]. A typical baffle arrangement consists of rigid radial and/or circumferential plates protruding perpendicularly from the injector plane. Wicker et al. [32] and You et al. [34] performed a thorough theoretical and numerical examination of three-dimensional chambers possessing radial and circumferential baffles. Acoustic waves become longitudinalized within the baffle compartments, and

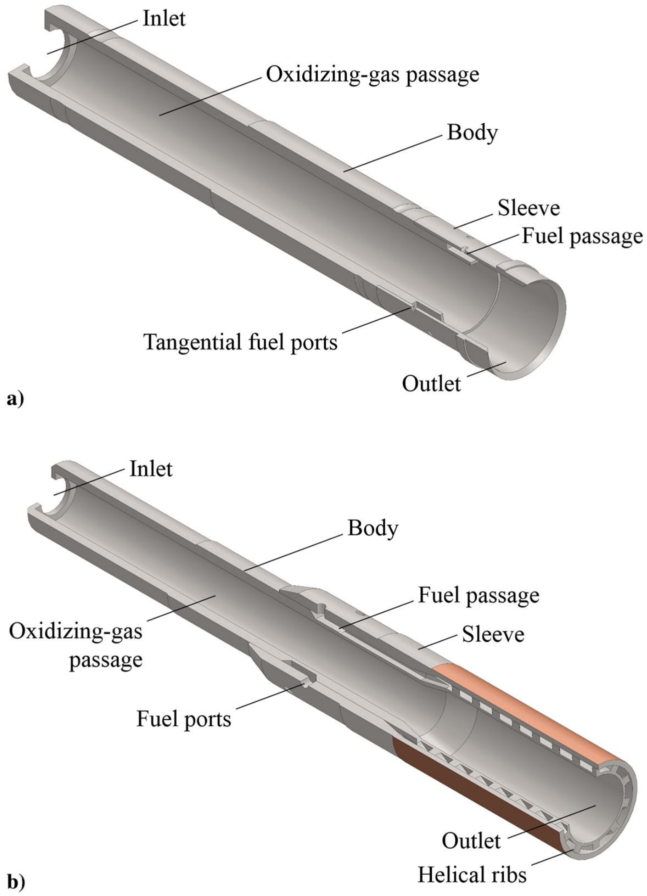

Fig. 2 Cross sections of a) main injector element and b) baffle injector element. Adapted from Yang et al. [10].

this may inhibit driving processes near the injector face that are sensitive to transverse pressure and velocity variations. Also, the addition of baffle blades reduces the frequency of oscillations by increasing the effective acoustic path length. Depending on the frequency spectrum of the combustion response, this may have either a stabilizing or destabilizing effect. Finally, it was noted that concentration of acoustic pressure occurs near the baffle tips, which may potentially destabilize the system. The effect of baffles is mainly geometric, and can be incorporated directly in the present formulation. Further description of the acoustic treatment of the flow distributor plate, nozzle, and injector manifold will be given in subsequent sections.

At the entrance to the oxidizing gas manifold is a distributor plate perforated with flow orifices. This component acts essentially as an acoustic liner. Such liners have been used widely in gas turbines and other devices to damp acoustic waves, and the theory describing their damping characteristics is well developed [35–37]. The mechanism of sound absorption may be described as follows. Acoustic waves incident on an orifice cause periodic shedding of vortices from the orifice rim. Some portion of the total incident energy is reflected, some transmitted, and some converted to the kinetic energy of the vortices. Unless the vortices impinge on a downstream obstacle and generate additional acoustic waves, they will eventually become incoherent turbulence. The magnitude of acoustic damping increases significantly in the presence of bias flow. The reflective properties of a single orifice may be quantified by the Rayleigh conductivity [35,37], which is defined as the ratio of the unsteady volume flux through the orifice to the applied unsteady pressure load. Assuming that the orifices are spaced widely enough that their shear layers do not interact (which is equivalent to specifying a low effective porosity), then the liner may be treated as a homogeneous compliant surface whose impedance can be built up from the impedance associated with each individual orifice.

The injectors themselves may provide a large amount of acoustic damping from a variety of mechanisms. As in the flow distributor, periodic vortex shedding is potentially significant, both at the inlet and outlet orifices. Of concern also is the direct visco-thermal dissipation of acoustic energy within the thin acoustic boundary layer. For a given frequency, the former dominates in the low Strouhal number (high amplitude) regime, whereas the latter dominates in the high Strouhal number (low amplitude) regime. The classical Kirchoff-Stokes theory [36,38,39] can be used to characterize these viscous losses in the case when the acoustic boundary layer is much thinner than the mean flow turbulent boundary layer. This mechanism is nominally present at all solid surfaces within the combustor, but may be particularly pronounced within the injectors both due to the large total surface area and the larger gradients in acoustic velocity. Searby et al. [29] incorporated this laminar dissipation mechanism by calculating an equivalent impedance and applying it as a boundary condition at the entrance plane of the resonator. An experimental investigation of injector damping by Lympany and Ahuja [40] incorporated viscous acoustic dissipation, but concluded that the key absorption mechanism for their rig was wave cancellation due to the coupling of acoustic modes between the injector and the surrounding chamber.

This paper is organized as follows. In Sec. II, an inhomogeneous wave equation characterizing acoustic oscillations is discussed, and theoretical models for various damping processes are developed. Section III presents results from a natural-mode analysis of the RD-170 thrust chamber assembly, followed by results incorporating the various damping processes in sequence. A discussion of the relative importance of each damping mechanism is then provided, along with suggestions for model improvements.

II. Methodology

A. Acoustic Wave Equation

Accounting for all the relevant physics in the two-phase reacting flow within a liquid rocket engine combustor is a complex task. The formulation originally established by Culick [24,41] begins with the conservation equations for mass, momentum, and energy written for both the gas and condensed phases in an idealized two-phase flow. Mass and momentum transfer due to phase changes are taken into account by source terms in the corresponding conservation equations. The mass-fraction equations for individual chemical species are not explicitly included in the formulation. Heat release due to combustion is accounted for as a source term in the energy equation, where it is assumed that a suitable reduced-order model may be obtained for this quantity. These equations are rearranged into a single set describing an equivalent gaseous system whose material properties are mass-weighted averages of those for the two phases present in the original system.

From the linearized conservation equations, the following generalized wave equation in the acoustic pressure is derived:

$$\frac{1}{\bar{\rho}\bar{c}^2}\frac{\partial^2 p'}{\partial t^2} - \frac{1}{\bar{\rho}}\nabla^2 p' = -\mathcal{M} + \frac{1}{\bar{\rho}}\nabla\cdot\boldsymbol{\mathcal{D}} \tag{1}$$

where the source terms have been collected into monopole sources, given by

$$\mathcal{M} = \frac{1}{\bar{\rho}\bar{c}^2}\left(\bar{\boldsymbol{u}}\cdot\nabla\frac{\partial p'}{\partial t} + \bar{\gamma}\frac{\partial p'}{\partial t}\nabla\cdot\bar{\boldsymbol{u}} + \frac{\partial(\boldsymbol{u}'\cdot\nabla p')}{\partial t} + \bar{\gamma}\frac{\partial(p'\nabla\cdot\boldsymbol{u}')}{\partial t} - \frac{\partial\mathcal{P}'}{\partial t}\right) \tag{2}$$

and dipole sources, given by

$$\boldsymbol{\mathcal{D}} = \bar{\rho}(\bar{\boldsymbol{u}}\cdot\nabla\boldsymbol{u}' + \boldsymbol{u}'\cdot\nabla\bar{\boldsymbol{u}}) + \left(\bar{\rho}\boldsymbol{u}'\cdot\nabla\boldsymbol{u}' + \rho'\frac{\partial\boldsymbol{u}'}{\partial t}\right) - \boldsymbol{\mathcal{F}}' \tag{3}$$

The boundary condition for Eq. (1) is obtained by taking the normal component of the momentum equation

$$-\frac{1}{\bar{\rho}}(\boldsymbol{n}\cdot\nabla p') = \boldsymbol{n}\cdot\frac{\partial \boldsymbol{u}'}{\partial t} + \boldsymbol{n}\cdot(\bar{\boldsymbol{u}}\cdot\nabla\boldsymbol{u}' + \boldsymbol{u}'\cdot\nabla\bar{\boldsymbol{u}} + \boldsymbol{u}'\cdot\nabla\boldsymbol{u}') + \boldsymbol{n}\cdot\left(\rho'\frac{\partial \boldsymbol{u}'}{\partial t}\right) + \boldsymbol{n}\cdot\boldsymbol{\mathcal{F}}' \tag{4}$$

The groups $\mathcal{P}'$ and $\boldsymbol{\mathcal{F}}'$ are not shown explicitly but, respectively, include contributions from chemical heat release and interphase momentum transfer. The terms contained in $\mathcal{M}$ are analogous to acoustic monopoles. Likewise the purely vector terms in $\boldsymbol{\mathcal{D}}$ are analogous to acoustic dipoles. There may also be second-order tensor terms that physically represent fluctuating shear stresses due, for example, to turbulence. These terms, analogous to quadrupole sources in classical acoustics, are neglected in this analysis. The radiation efficiency of such sources is uniformly small for the frequency range considered. It should be noted that combustion, although not considered in detail in this work, is generally incorporated as a monopole source.

Because the present analysis is concerned with linear stability, all second-order terms in Eqs. (1–3) are discarded. We assume that the unsteady pressure and velocity vary harmonically as $p' = \hat{p}e^{i\Omega t}$ and $\boldsymbol{u}' = \hat{\boldsymbol{u}}e^{i\Omega t}$, respectively, where $\hat{p}$ and $\hat{\boldsymbol{u}}$ represent complex spatial amplitudes. The complex frequency is expressed as $\Omega = \omega + i\alpha$. Note that this sign convention implies $e^{i\Omega t} = e^{i\omega t}e^{-\alpha t}$, such that a positive value for the growth constant indicates a damped wave. Neglecting chemical source terms and two-phase coupling terms,

$$-\frac{1}{\bar{\rho}}\left(\frac{\Omega^2}{\bar{c}^2}\hat{p} + \nabla^2\hat{p}\right) = -\frac{i\Omega}{\bar{\rho}\bar{c}^2}(\bar{\boldsymbol{u}}\cdot\nabla\hat{p} + \bar{\gamma}\,\hat{p}\,\nabla\cdot\bar{\boldsymbol{u}}) + \nabla\cdot(\bar{\boldsymbol{u}}\cdot\nabla\hat{\boldsymbol{u}} + \hat{\boldsymbol{u}}\cdot\nabla\bar{\boldsymbol{u}}) \tag{5}$$

$$-\frac{1}{\bar{\rho}}(\boldsymbol{n}\cdot\nabla\hat{p}) = i\Omega(\boldsymbol{n}\cdot\hat{\boldsymbol{u}}) + \boldsymbol{n}\cdot(\bar{\boldsymbol{u}}\cdot\nabla\hat{\boldsymbol{u}} + \hat{\boldsymbol{u}}\cdot\nabla\bar{\boldsymbol{u}}) \tag{6}$$

Introducing the acoustic impedance $Z \equiv \hat{p}/(\boldsymbol{n}\cdot\hat{\boldsymbol{u}})$, the boundary condition (6) may be expressed as

$$-\frac{1}{\bar{\rho}}(\boldsymbol{n}\cdot\nabla\hat{p}) = (i\Omega + \bar{\boldsymbol{u}}\cdot\nabla + \boldsymbol{n}\cdot\nabla\bar{\boldsymbol{u}}\cdot\boldsymbol{n})\frac{\hat{p}}{Z}$$

which is equivalent to the boundary condition of Myers [42]. In this form, it is capable of describing an impedance surface over which there is a spatially nonuniform slip velocity.

In the present study, we consider a simplified model for the mean flow. We impose a uniform, purely axial flow in each region, with velocity magnitudes determined from the mass flow rates specified by the RD-170 design. With this specification, only a single monopole term survives from (5), leaving

$$-\frac{1}{\bar{\rho}}\left(\frac{\Omega^2}{\bar{c}^2}\hat{p} + \nabla^2\hat{p}\right) = -\frac{i\Omega}{\bar{\rho}\bar{c}^2}\bar{\boldsymbol{u}}\cdot\nabla\hat{p} \tag{7}$$

Finally, in the absence of mean flow, the system reduces to

$$-\frac{1}{\bar{\rho}}\left(\frac{\Omega^2}{\bar{c}^2}\hat{p} + \nabla^2\hat{p}\right) = 0 \tag{8}$$

subject to the boundary condition

$$-\frac{1}{\bar{\rho}}(\boldsymbol{n}\cdot\nabla\hat{p}) = i\Omega\frac{\hat{p}}{Z} \tag{9}$$

For solid walls with $Z \to \infty$, the classical Helmholtz equation for the normal modes of a chamber is recovered. Equations (8) and (9) are used to compute the chamber eigenmodes, while Eqs. (7) and (9) are used to compute the acoustic mode in the presence of the imposed mean flow. The effects of different source terms and boundary conditions are then explored systematically.

Table 1 Gas properties at chemical equilibrium conditions for RD-170 engine

Parameter	GOX manifold	Main chamber
O/F ratio	52.31	2.60
Equivalence ratio	0.066	1.32
Temperature, K	687.7	3676.1
Pressure, bar	270	245.5
Heat capacity ratio	1.33	1.2
Enthalpy, kJ/kg	−463.31	−1644.54
Entropy, kJ/(kg · K)	5.876	10.64
Constant pressure heat capacity, J/(kg · K)	1056.40	2035.65
Specific gas constant, J/(kg · K)	260.56	343.43
Molecular weight, g/mole	31.91	24.21
Density, kg/m^3	150.70	19.45
Sound speed, m/s	487.5	1231.9
Kinematic viscosity $\times10^{-6}$, m^2/s	0.243	5.26
Thermal conductivity, W/(m · K)	0.048	0.290
Thermal diffusivity $\times10^{-6}$, m^2/s	0.3	7.32

B. Gas Properties

The GOX manifold and injectors are assumed to contain only oxidizer, whereas the main combustion chamber is assumed to contain only the equilibrium products of combustion at the adiabatic flame temperature (all conductive heat losses from chamber walls are ignored). The liquid fuel used is RP-1 kerosene, a mixture of various hydrocarbons with an overall ratio of hydrogen to carbon atoms of approximately 1.9423. For simplicity, $C_{12}H_{24}$ (dodecane), which has comparable thermophysical properties, may be used as a surrogate fuel [43]. Correlations for the specific heat capacity, sensible enthalpy, and other quantities used in the equilibrium calculation can be found in the work of Svehla [44]. The calculated gas properties are given in Table 1. The temperatures in the preburner and main chamber are taken as spatially uniform.

C. Nozzle Impedance

The analysis includes the entire converging portion of the nozzle. An impedance condition must be applied at the sonic plane. Of central interest in this study are the lowest transverse (1T and 2T) modes. Bell and Zinn [45] and Zinn et al. [46] conducted theoretical and numerical studies of the acoustic admittances of liquid rocket thrust chamber nozzles for mixed longitudinal-transverse modes, and found that both the real and imaginary parts of the admittances are close to zero. The nozzle essentially behaves like an acoustically rigid boundary.

D. Flow Distributor Impedance

At the entrance to the GOX chamber is a flow distributor, as shown in Fig. 3. This structure serves mainly to ensure that the GOX flow

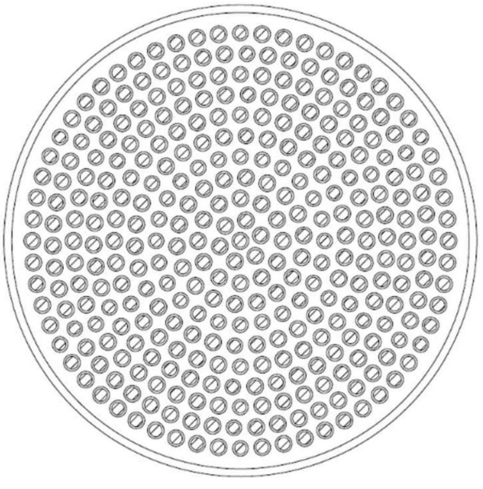

Fig. 3 Flow distributor plate from RD-170 engine. Adapted from Yang et al. [10].

entering the injector manifold is relatively uniform, and it offers the additional benefit of damping incident acoustic waves. The irregular spatial arrangement of orifices and the curvature of the plate complicate the acoustic analysis. It is assumed that the radius of curvature of the plate is large relative to an acoustic wave length, such that it can be considered approximately planar. Each orifice of radius R is separated by a distance d from its closest neighbors as shown in Fig. 4. A bias flow of an average velocity u_c traverses each orifice.

The plate is assumed to be infinitesimally thin, so that it is only a matching interface between two otherwise unbounded regions. Interrogation of this assumption by Jing and Sun [47] confirms that the thickness of a liner may safely be neglected if the bias flow Mach number is sufficiently high. Let the acoustic field in the region $x > 0$, p'_+, consists of an incident and reflected harmonic plane wave, and the field in the region $x < 0$, p'_-, consists of a transmitted plane wave:

$$p'_+(x, y, t) = (e^{ik_1x - ik_2y} + \mathcal{R}e^{-ik_1x - ik_2y})e^{i\omega t} \tag{10}$$

$$p'_-(x, y, t) = \mathcal{T}e^{ik_1x - ik_2y}e^{i\omega t} \tag{11}$$

where $k_1 = k\cos\theta$, $k_2 = k\sin\theta$, and $k = \omega/\bar{c}$ is the wave number. The fields obey the following matching conditions at the plate [36]:

$$\left.\frac{\partial p'_-}{\partial x}\right|_{x=0} = \mathcal{N}\chi(p'_+ - p'_-)|_{x=0} \tag{12}$$

$$\left.\frac{\partial p'_+}{\partial x}\right|_{x=0} = \mathcal{N}\chi(p'_+ - p'_-)|_{x=0} \tag{13}$$

where $\mathcal{N}$ is the number density of orifices on the plate, and χ is the Rayleigh conductivity of an orifice. Enforcement of these conditions on Eqs. (10) and (11) reveals

$$\mathcal{R} = \frac{k_1}{k_1 + 2i\mathcal{N}\chi} \tag{14}$$

Note that only the component of the incident wave normal to the screen participates is reflected. This may be related to the impedance by

$$Z = \frac{1 + \mathcal{R}}{1 - \mathcal{R}}\frac{\bar{\rho}\,\bar{c}}{\cos\theta}$$

to yield

$$\frac{Z}{\bar{\rho}\,\bar{c}} = \frac{1}{\cos\theta} + \frac{kd^2}{i\chi} \tag{15}$$

where, for the square arrangement of orifices used in this example, the number density has been expressed as $\mathcal{N} = 1/d^2$. Various physical models may be developed for the Rayleigh conductivity. The classical model of Howe [35] produces a conductivity of the form $\chi = 2R(\gamma - i\delta)$, where the functions γ and δ depend on the orifice radius, bias flow velocity, and the frequency of the incident acoustic wave in the following way:

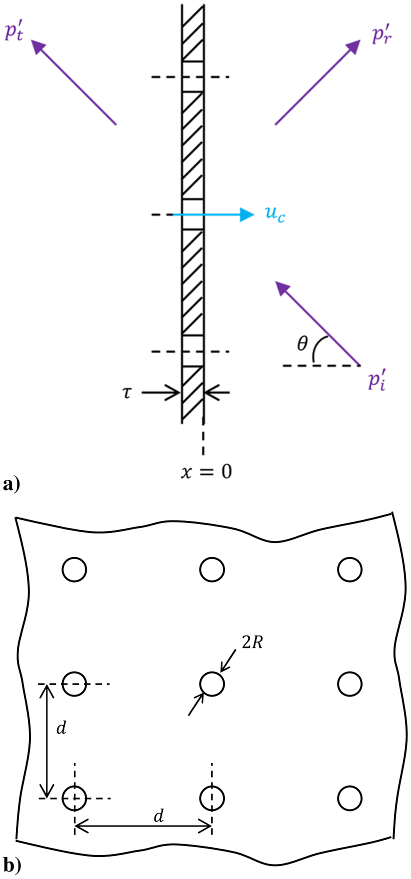

Fig. 4 a) Side and b) front views of idealized perforated plate model.

$$\gamma = \frac{I_1(k_cR)[1 + (1/k_cR)] + (4/\pi^2)e^{2k_cR}\cosh(k_cR)K_1(k_cR)^2[\cosh(k_cR) - (\sinh(k_cR)/k_cR)]}{I_1(k_cR)^2 + (4/\pi^2)e^{2k_cR}\cosh^2(k_cR)K_1(k_cR)} \tag{16}$$

$$\delta = \frac{(2/\pi k_cR)I_1(k_cR)K_1(k_cR)e^{2k_cR}}{I_1(k_cR)^2 + (4/\pi^2)e^{2k_cR}\cosh^2(k_cR)K_1(k_cR)^2} \tag{17}$$

where I_1 and K_1 denote modified Bessel functions of order 1 of the first and second kind, respectively, and $k_c = \omega/u_c$ is a convective wave number. The linearized theory that produces these expressions is predicated on the assumption of a high Reynolds number bias flow. In this case, the flow may be approximated as inviscid in every region except an infinitely thin cylindrical vortex sheet shed from the orifice rim. The functions γ and δ are plotted in Fig. 5. Note the behavior in the two important limits $k_cR \to 0$ and $k_cR \to \infty$. In the former case, which corresponds to either low frequency or high bias flow velocity, the conductivity approaches zero and the liner approximates an acoustically rigid boundary. On the other hand in the high k_cR

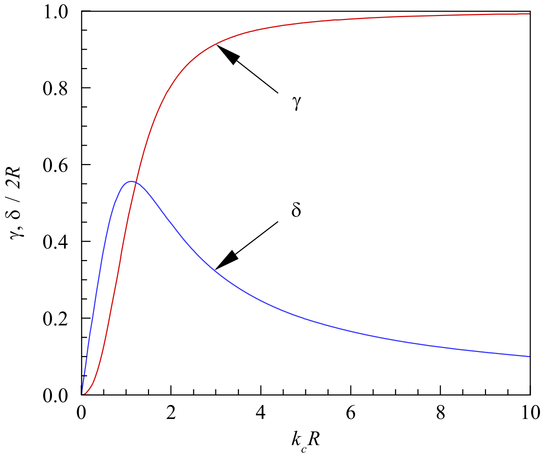

Fig. 5 Real and imaginary parts of Rayleigh conductivity as a function of nondimensionalized wave number.

limit, which corresponds to either high frequency or low bias flow velocity, $\chi \to 2R$ as expected from classical potential theory [36].

The flow distributor plate considered here is perforated by orifices of radius $R = 3.5$ mm, separated by an average distance of $d = 1.2$ cm. A bias flow of average magnitude $u_c = 121.6$ m/s traverses each orifice. Because only the normal wave components participate in the reflection, attention is restricted to the case $\theta = 0$. The corresponding impedance computed from Eq. (15) is shown in Fig. 6 over a 10 kHz frequency range. For frequencies less than about 4 kHz, the impedance is approximately constant. The liner, however, behaves like a strongly reflective surface with phase delay at high frequencies.

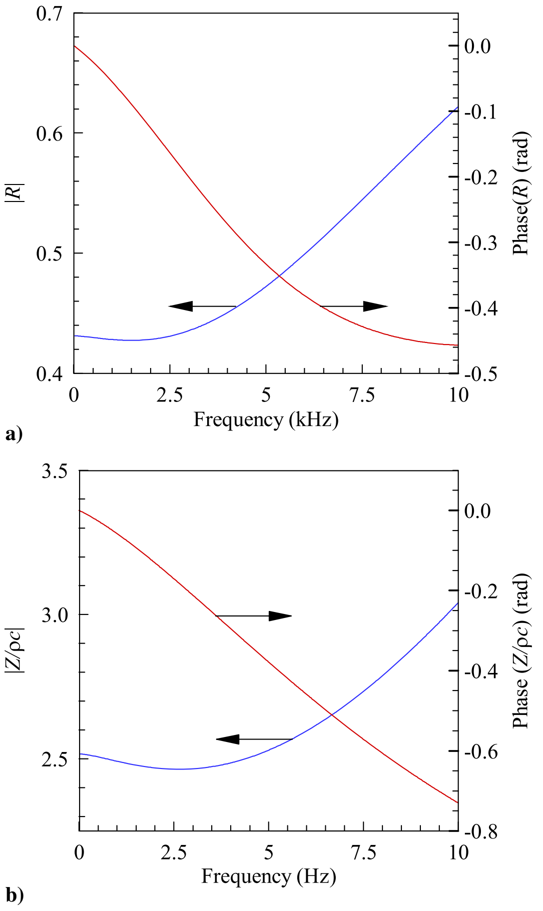

Fig. 6 Magnitude and phase of a) reflection coefficient and b) normalized impedance of flow distributor plate.

E. Injector Damping

For simplicity, the presence of any liquid film within the injectors is ignored, and the volume is assumed to be filled entirely with gaseous oxidizer. The two principal acoustic damping mechanisms under consideration are 1) viscous damping of acoustic waves and 2) energy transfer from the acoustic to the vortical mode at inlet and outlet orifices. The relative importance of these mechanisms may be estimated in terms of the Strouhal number $St_\omega = \omega R/\hat{u}$, where $\hat{u}$ is the amplitude of the acoustic velocity and R is the injector radius [29]. If $St_\omega \gg 1$, viscous dissipation dominates the damping. Figure 7 shows schematically the gas volumes enclosed by both main and baffle injector elements. The main injection element includes a portion of the gas volume within the countersunk bores on the injector face.

An equivalent impedance can be derived for the injection surface by taking into account viscous dissipation [36,39]. For a wave incident at an angle θ, we have

$$\frac{Z}{\bar{\rho}\,\bar{c}} = e^{i\pi/4}\sqrt{\frac{\bar{c}^2}{\omega\nu}}\left(\sin^2\theta + \frac{\bar{\gamma} - 1}{\sqrt{Pr}}\right)^{-1} \tag{18}$$

The factor $e^{i\pi/4} = (1+i)/\sqrt{2}$ indicates that both the real and imaginary parts of the impedance are the same, and the phase is a constant. Thus the amplitude may simply be taken as either $\sqrt{2}\mathrm{Re}\{Z\}$ or $\sqrt{2}\mathrm{Im}\{Z\}$. For the gas properties presented in Table 1, Fig. 8 shows the frequency variation of the impedance.

The impedance remains high for the entire frequency range of concern, and in particular $|Z| \to \infty$ as $f \to 0$. In the presence of viscous dissipation within the acoustic boundary layers, a variational analysis incorporating Eq. (18) shows that the wave number for quasi-plane waves propagating in a duct of radius R can be expressed as

$$k_v = \frac{\omega}{\bar{c}} + \frac{e^{-i\pi/4}}{R}\sqrt{\frac{\omega\nu}{\bar{c}^2}}\left(1 + \frac{\bar{\gamma} - 1}{\sqrt{Pr}}\right) \tag{19}$$

These results are valid provided the acoustic boundary layer remains laminar. At high Reynolds numbers additional damping may arise due to turbulence penetrating the acoustic boundary layer [48,49], and in that case corrected damping models should be employed.

We define a complex speed of sound $\bar{c}_v \equiv \omega/k_v$, and a complex density $\rho_v \equiv k_v Z/\omega$. Utilizing these gas properties in the computation

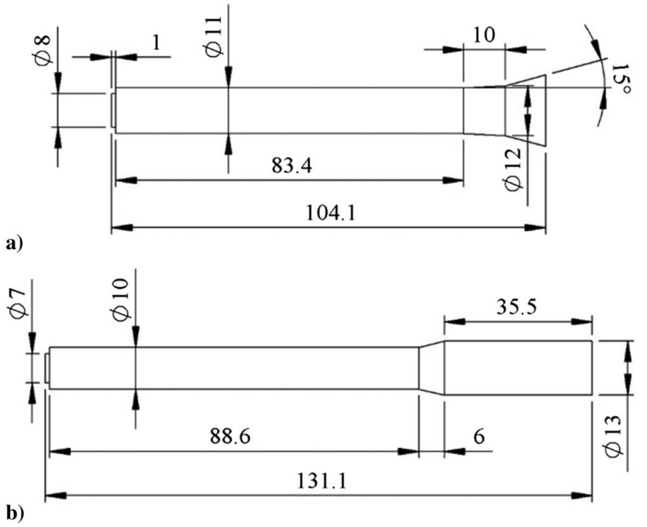

Fig. 7 a) Main injector element dimensions. b) Baffle injector elements (all dimensions in mm).

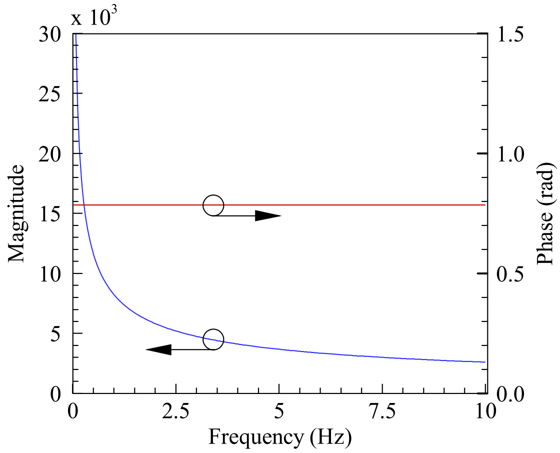

Fig. 8 Equivalent impedance of acoustic boundary layer $Z/\bar{\rho}\,\bar{c}$ as seen by plane waves at grazing incidence.

accounts indirectly for the presence of viscous damping and circumvents the numerical difficulties of direct application of Eq. (18) to the injection surface.

III. Results and Discussion

A. Normal Acoustic Modes

As a baseline, the normal acoustic mode shapes and frequencies of the main combustion chamber of the RD-170 engine are determined by an eigenvalue analysis of the system (8) and (9) with rigid boundaries ($Z = \infty$). The first tangential (1T) and second tangential (2T) modes are known to dominate, and so are the focus of the present results [9]. Figures 9–15 show results for these modes, for both baffled and unbaffled injectors. Because the amplitudes in a linear analysis are arbitrary, in all figures the pressure and velocity amplitudes have been suitably normalized to unity. Also, note that different cross sections of the chamber are used to display different modes. This is because the spatial orientation of the transverse modes does not correlate with one another and so different cross sections must be chosen to display the antinodes in each case. The calculated natural frequencies are listed in Table 2.

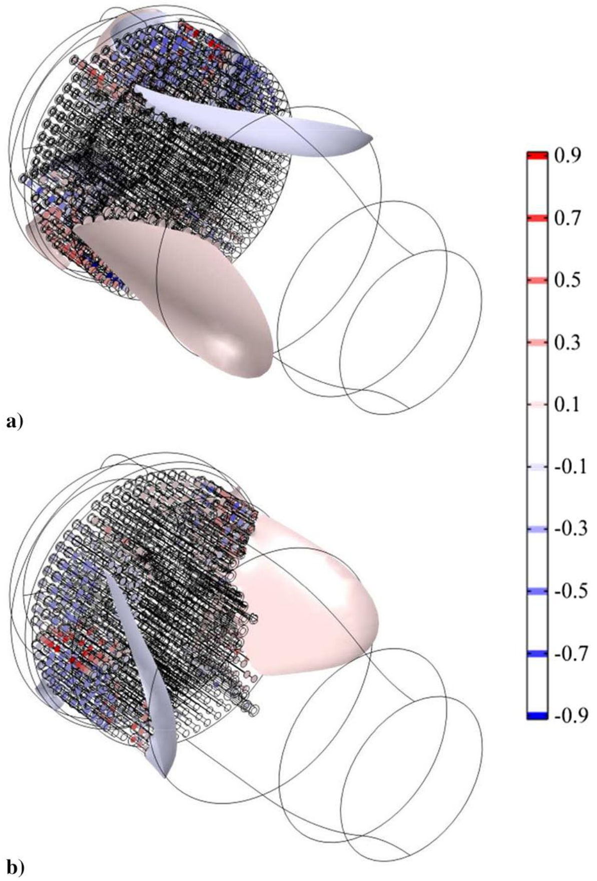

Fig. 9 Pressure isosurfaces for the 1T (1881 Hz) mode: a) unbaffled configuration; b) baffled configuration.

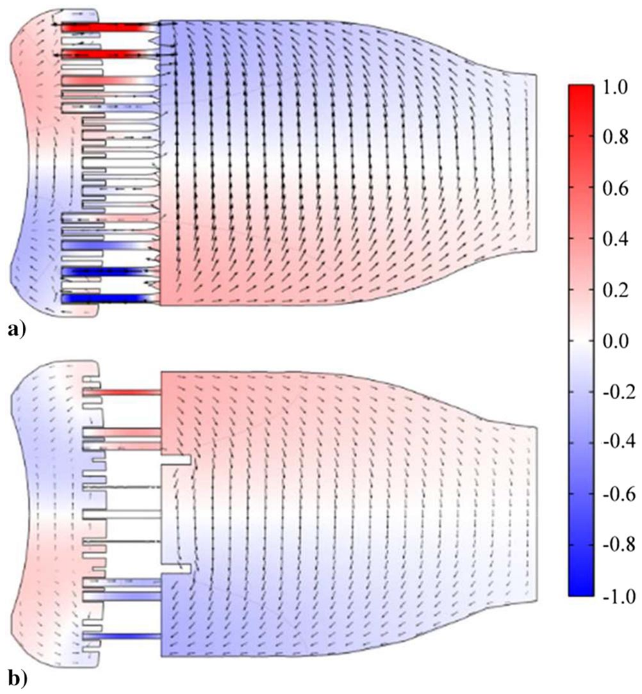

Fig. 10 Pressure and velocity fields of first (1T) tangential modes at maximum longitudinal cross section: a) unbaffled configuration; b) baffled configuration.

The addition of baffles slightly decreases the frequency of oscillation, a result consistent with findings from previous studies. For the chamber and injection geometries considered here, the approximate formula of Dranovsky et al. [9] predicts a decrease of about 1% in the natural frequency with the addition of baffles, in reasonable agreement with the results in Table 2.

The acoustic waves are longitudinal within the injectors, with their amplitude attaining a maximum value. The waves become slightly longitudinalized within the baffle compartments, and acoustic pressure is more concentrated near the injector plane for the baffled configuration. A similar observation was made by You et al. [34] in the study of acoustic waves in baffled combustors.

The baffled and unbaffled model geometries in Figs. 9a and 9b, respectively, are oriented identically in space, as are those in Figs. 12a and 12b. The addition of baffles alters the preferred spatial orientation of the acoustic mode for both the 1T and 2T modes. A more detailed study of this phenomenon, including the dynamics of spinning acoustic waves in baffled combustion chambers, is needed.

B. Flow Distributor Damping

Equation (15) can be expanded to render an explicit function of frequency and used as a boundary condition. This approach, however, is cumbersome for an iterative solver. Instead, nominal constant values of the impedance based on the natural frequencies are determined in advance and used as the boundary condition. Equations (8) and (9), now with Z specified using the impedance model (15), are solved. The values for the impedance are shown in Table 3, along with the nominal eigenmode frequencies from the previous section used as inputs to the impedance model. Table 4 shows the corresponding damped eigenvalue results. Note that in reality the oscillation frequency and boundary conditions are mutually dependent on each other; the problem is coupled and must

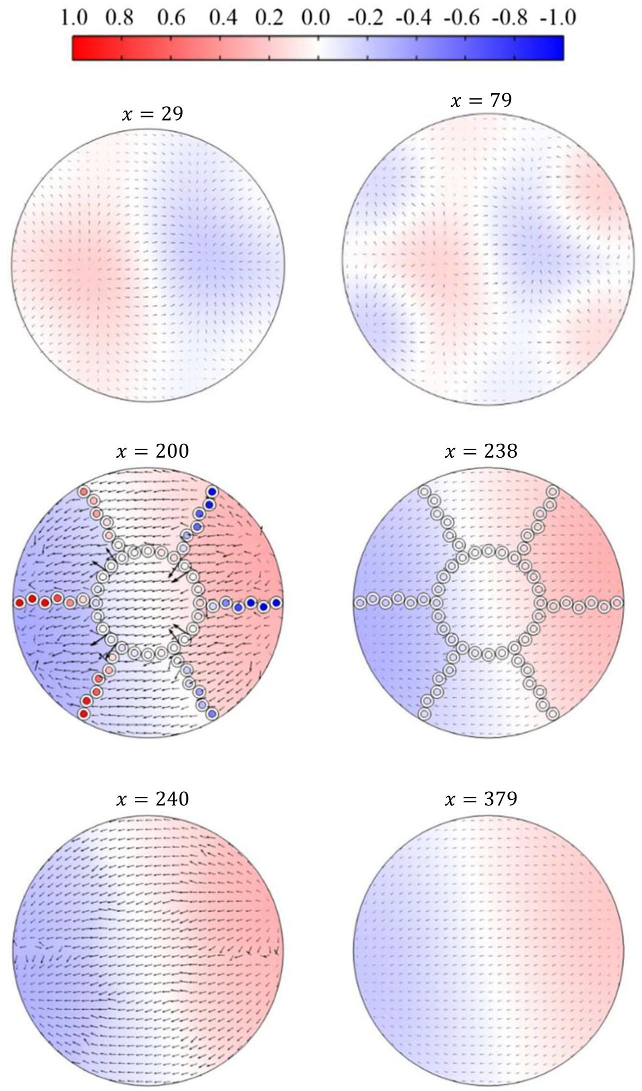

Fig. 11 Axial cross sections of pressure and velocity fields for first tangential (1T) mode (all dimensions in mm).

be solved iteratively. The change in frequency due to damping effects, however, is generally negligible, and the errors introduced by fixing an impedance value are expected to be small. Figures 16–18 show the acoustic pressure and velocity fields of the first and second tangential modes for the rigid and impedance boundary conditions, respectively. For brevity, only the longitudinal cross sections are presented. No discernible difference in the mode shape between the two different boundary conditions is observed.

The damping of the 2T mode is noticeably less than that of the 1T mode. This is attributable partially to the frequency dependence of the impedance, and partially to the nature of transverse oscillations in the oxidizer manifold. Owing to the small axial extent of the oxidizer plenum, the higher-order transverse oscillations translate to a lower average angle of incidence between the incident waves and the distributor plate.

C. Injector Damping

As described in Sec. II.E, the Strouhal number $\omega R/\hat{u}$ is used to estimate the damping mechanism within injectors. The acoustic velocity is selected by assuming that the acoustic pressure $\hat{p}$ is 1% of the mean pressure, a condition valid for a linear acoustic analysis. Tables 5 and 6 present some relevant flow variables for both injectors. Gas properties are taken from Table 1, where needed.

Note that the Mach number remains small throughout the injector except in the thin inlet orifice. The Strouhal numbers exceed unity over the entire injector, which suggests that for small amplitudes within the linear acoustic regime, viscous dissipation dominates the acoustic damping of the injectors. The situation may become different when oscillations become so strong that the

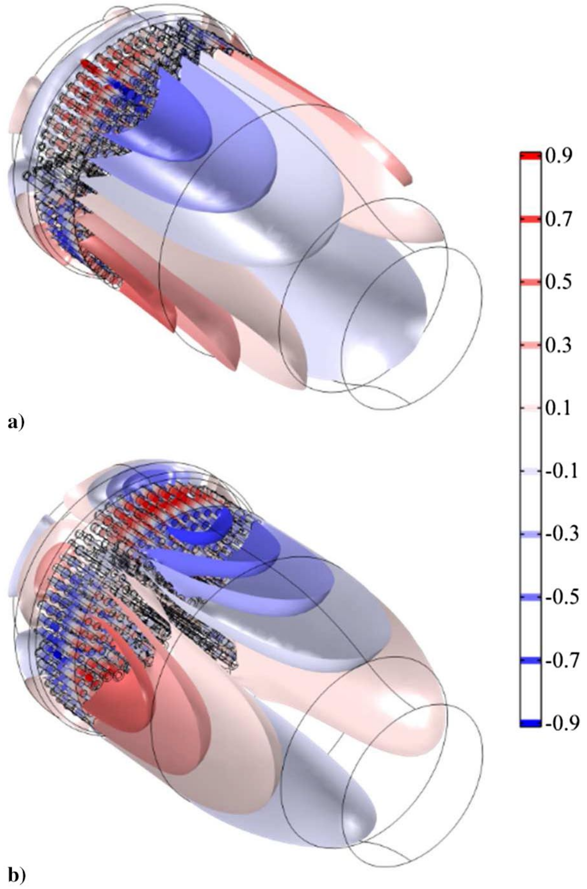

Fig. 12 Pressure isosurfaces for second tangential (2T) mode: a) unbaffled configuration; b) baffled configuration.

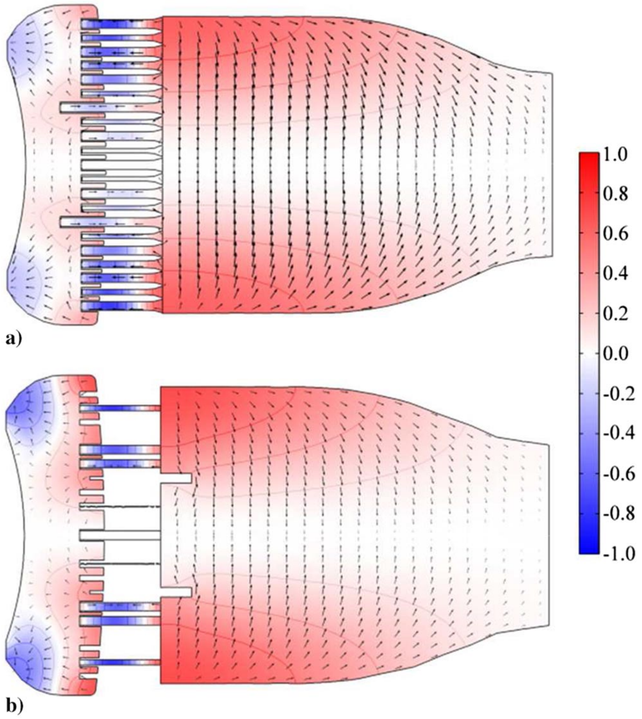

Fig. 13 Pressure and velocity fields of second tangential (2T) mode at 0° longitudinal cross section: a) unbaffled configuration; b) baffled configuration.

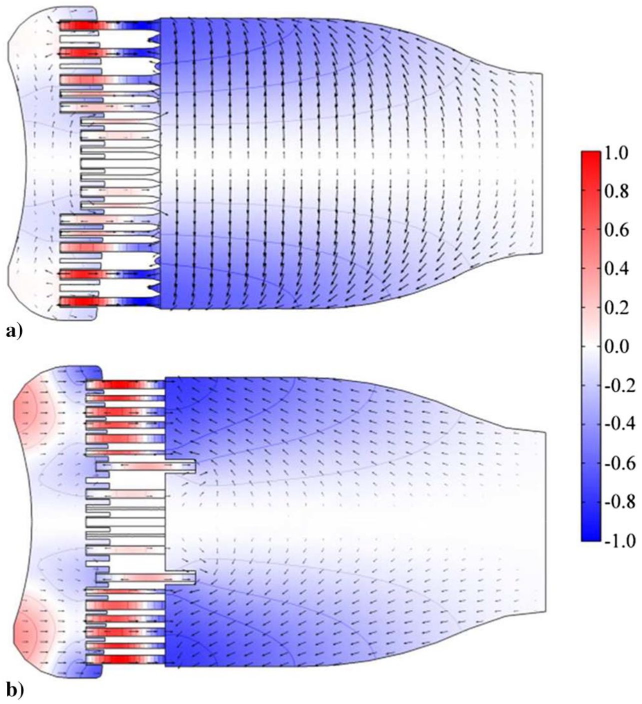

Fig. 14 Pressure and velocity fields of second tangential (2T) mode at 90° longitudinal cross section: a) unbaffled configuration; b) baffled configuration.

energy transfer from the acoustic to the vortical mode prevails. Under that condition, both viscous dissipation and acoustic-viscous interaction should be considered to account for the acoustic damping of injectors.

In the present analysis, an impedance model for laminar viscous dissipation is implemented. Such an impedance model was applied in Searby et al. [29] to account for the viscous damping within a resonator bank; it was applied as a lumped resistive layer at the entrance plane of the bank. In the current study, the injectors are included as part of the computational domain, and the impedance is applied along the interior surface of the injector. Further, only longitudinal acoustic motions are expected in the injectors because the radius is small. The impedance (18) is thus specified to the case $\theta = 90°$. Table 7 gives the values employed for the equivalent density and speed of sound based on the normal frequencies of the 1T and 2T modes, and Table 8 shows the effect on frequency and growth rate. Figures 19–21 show the 1T and 2T mode shapes resulting from the solution of Eqs. (8) and (9) with the indicated gas properties for cases with and without injector damping.

Again the damping of the 2T mode is lower than that of the 1T mode. However in this instance, the effect of frequency dependence predominates. Because the viscous damping is applied only within the injectors, and because in all cases the acoustic motions are completely longitudinalized in this region, there is unlikely to be a significant difference associated with acoustic mode shape. Increasing the length of the injectors would straightforwardly increase the damping by virtue of the larger surface area over which the viscous stresses act. However, this would potentially come at the expense of reduced injector performance due to unwanted flow losses.

D. Mean Flow

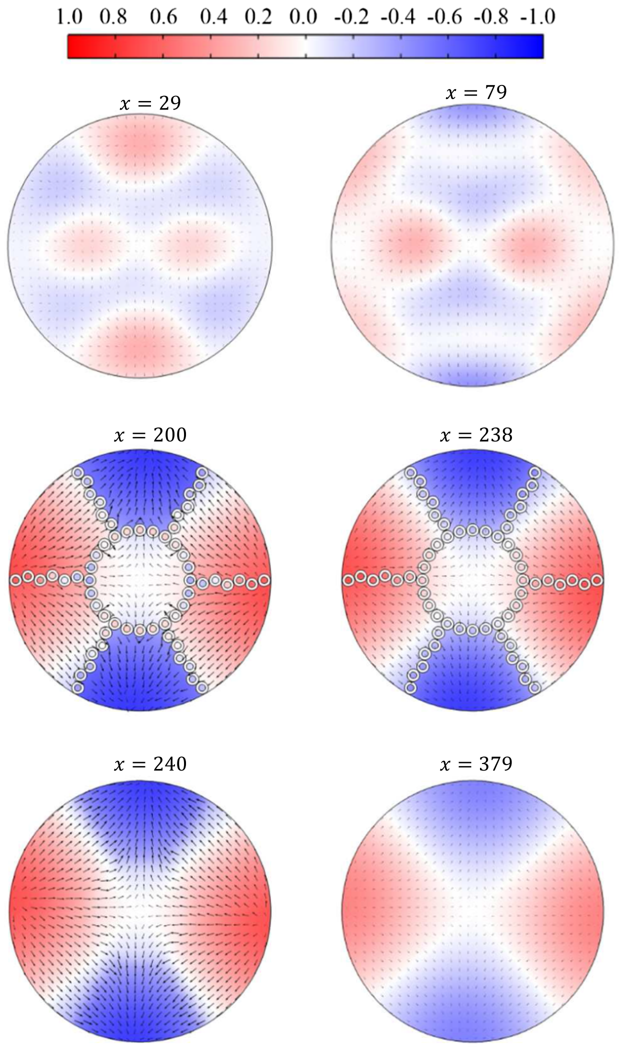

Fig. 15 Axial cross sections of pressure and velocity fields for second tangential (2T) mode (all dimensions in mm).

The effects of mean flow are examined by specifying a uniform, axial flow speed U. All solid surfaces are specified as acoustically closed ($Z \to \infty$), so as to isolate the effects of mean flow, rather than to elucidate the coupling of mean flow with impedance surfaces. Thus, the eigenmode problem is now governed by Eqs. (7) and (9). The mean flow velocity U is applied piecewise with three nominal values: 17.63 $\mathrm{m/s}$ in the oxidizer dome, 93.4 $\mathrm{m/s}$ within the injectors, and 326.9 $\mathrm{m/s}$ in the main chamber, in accordance with the flow conditions in the RD-170 engine. These values were determined based on mass flow rate analysis for the RD-170. Figures 22–24 show the 1T and 2T modes of acoustic pressure and velocity for cases with and without mean flow effects. Table 9 gives

Table 2 Normal frequencies (Hz) of RD-170 main combustion chamber

Mode	Unbaffled	Baffled
1T	1908	1881
2T	3217	3152

Table 3 Nominal flow-distributor impedances applied for each mode

Mode	Frequency, Hz	Normalized impedance
1T	1880	$2.624 - 0.365i$
2T	3150	$2.569 - 0.667i$

Table 4 Effect of flow distributor impedance on frequency and damping coefficient

Mode	Mode frequency, Hz	Damped frequency, Hz
1T	1880	$1886 + 6.6i$
2T	3150	$3151 + 1.8i$

the calculated frequencies and damping coefficients of the acoustic oscillations.

The damping provided by the mean flow appears to be significantly larger than other effects. The damping coefficient increases from 6.6 to 32.4 for the 1T mode and from 1.8 to 53.5 for the 2T mode, as compared with the contributions from the flow distributor. The oscillation frequency is slightly reduced from the no-flow case, in qualitative agreement with modal theories [50,51]. The large damping resulting from the mean flow may be attributable to convective losses of acoustic energy. Even in the case of a perfectly reflective exit plane (such as that employed here), acoustic energy is convected out by the mean flow, and the acoustic energy in the system is reduced.

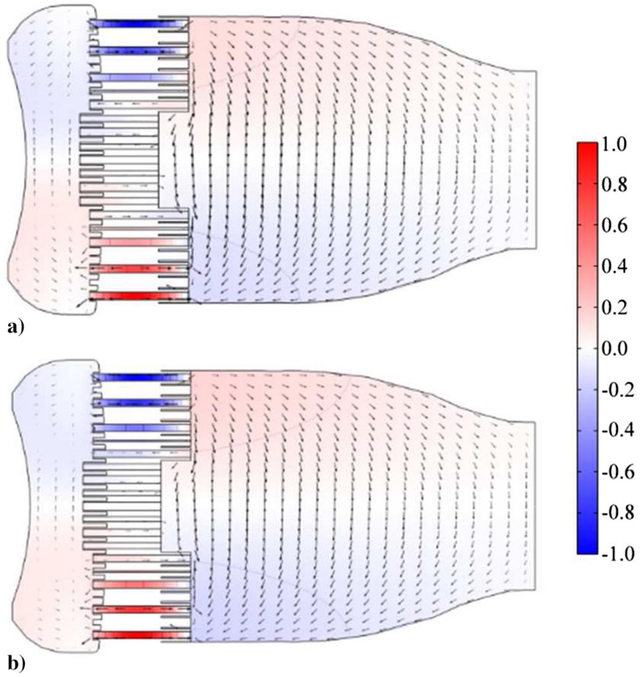

Fig. 16 First tangential (1T) mode shapes of acoustic pressure and velocity 0° longitudinal cross section for a) rigid and b) impedance flow distributor boundary conditions.

This effect may be further explained with a calculation for an analogous cylindrical chamber. Consider a chamber of radius R with a uniform mean flow of Mach number M. The pressure and axial velocity fields may be constructed as superpositions of known eigensolutions as follows

$$p'(x,r,\theta,t) = e^{i\Omega t} \sum_{n=-\infty}^{\infty} \sum_{m=0}^{\infty} J_n\left(\frac{\alpha_{nm} r}{R}\right) e^{in\theta}\left[P_{nm}^{+} e^{ik_{nm}^{+}x} + P_{nm}^{-} e^{ik_{nm}^{-}x}\right] \tag{20}$$

$$u'(x,r,\theta,t) = -\frac{1}{\bar{\rho}\,\bar{c}} e^{i\Omega t} \sum_{n=-\infty}^{\infty} \sum_{m=0}^{\infty} J_n\left(\frac{\alpha_{nm} r}{R}\right) \times e^{in\theta}\left[\frac{P_{nm}^{+} k_{nm}^{+} e^{ik_{nm}^{+}x}}{k + M k_{nm}^{+}} + \frac{P_{nm}^{-} k_{nm}^{-} e^{ik_{nm}^{-}x}}{k + M k_{nm}^{-}}\right] \tag{21}$$

where J_n denotes the Bessel function of the first kind of order n, α_{nm} the mth root of $J_n'(r)$, and

$$k_{nm}^{\pm} = \frac{kM \mp \sqrt{k^2 - (\alpha_{nm}/R)^2(1 - M^2)}}{1 - M^2}$$

The power transmitted axially by the acoustic field is given by the area integral of the axial acoustic intensity over the cross-sectional area of the chamber:

$$\mathcal{P} = \int_S \langle \boldsymbol{I} \cdot \boldsymbol{e}_x \rangle \, \mathrm{d}S$$

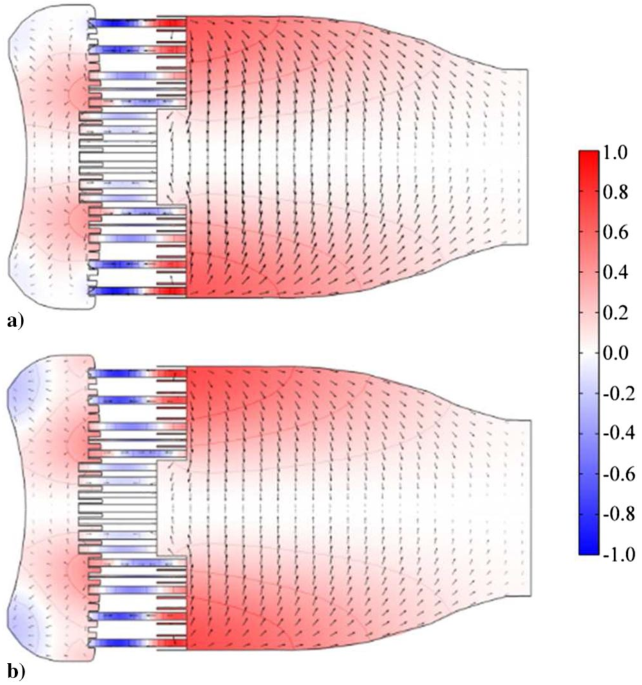

Fig. 17 Second tangential (2T) mode shapes of acoustic pressure and velocity 0° longitudinal cross section for a) rigid and b) impedance flow distributor boundary conditions.

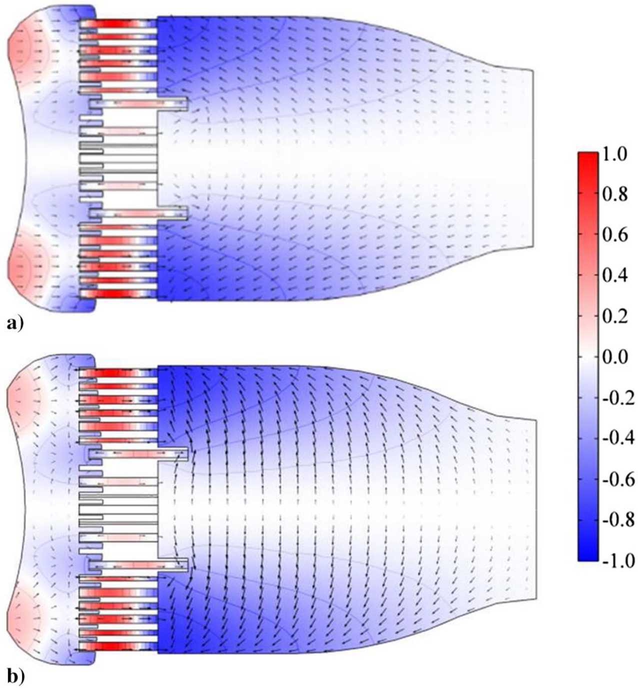

Fig. 18 Second tangential (2T) mode shapes of acoustic pressure and velocity 90° longitudinal cross section for a) rigid and b) impedance flow distributor boundary conditions.

Table 5 Dimensions and flow parameters for main injector element

Axial location	R, mm	St_ω (1T)	St_ω (2T)
Inlet orifice	4.00	4.50	7.54
Main passage	5.50	6.19	10.38
Diverging outlet 1	6.00	6.75	11.32
Diverging outlet 2	8.87	9.98	16.73

Table 6 Dimensions and flow parameters for baffle injector element

Axial location	R (mm)	St_ω (1T)	St_ω (2T)
Inlet orifice	3.50	3.94	6.60
Main passage	5.00	5.63	9.43
Second passage	6.50	7.32	12.26

Table 7 Equivalent gas properties used for characterizing injector damping

Mode	Frequency (Hz)	Complex density $\rho_v\cdot(\mathrm{kg/m^3})$	Speed of sound c_v (m/s)
1T	1880	$32.3-0.785i$	487.3
2T	3150	$25-0.785i$	487.34

Table 8 Effect of injector damping on frequency and damping coefficient

Mode	Mode frequency (Hz)	Damped frequency (Hz)
1T	1880	$1868+7.08i$
2T	3150	$3210+3.14i$

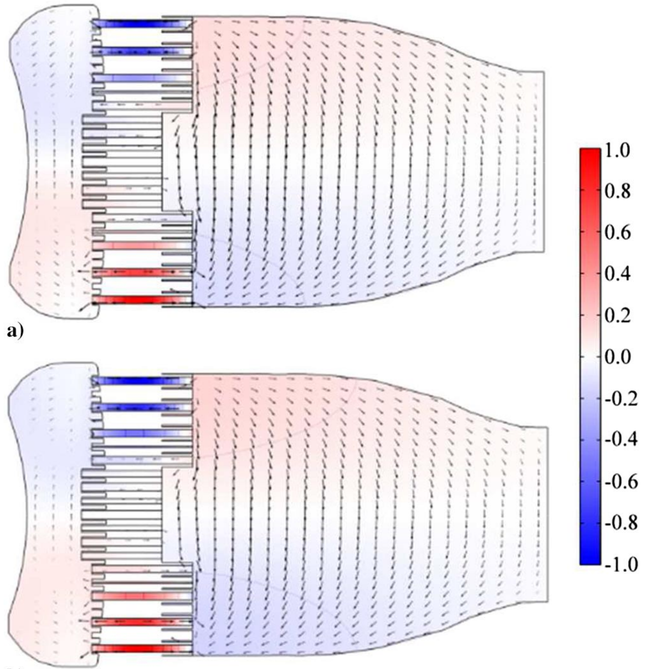

Fig. 19 First tangential (1T) mode shapes of acoustic pressure and velocity 0° longitudinal cross section a) with and b) without injector damping.

Using the expressions for pressure and velocity, this ultimately yields

$$\mathcal{P}=\frac{\pi R^2}{\bar{\rho}\,\bar{c}}(1-M^2)^2\sum_{n=-\infty}^{\infty}\sum_{m=0}^{m_0}J_{n+1}(\alpha_{nm})^2\times\sigma_{nm}\left[\frac{|P^+_{nm}|^2}{(1-M\sigma_{nm})^2}-\frac{|P^-_{nm}|^2}{(1+M\sigma_{nm})^2}\right]\tag{22}$$

where m_0 denotes the number of cut on modes. The nondimensional group σ_{nm} is defined as $\sqrt{1-(\alpha_{nm}/kR)^2(1-M^2)}$. Residual contributions from coupled evanescent modes are omitted.

Let us consider the contribution for a single arbitrary mode. We retain the only contribution of the downstream propagating wave, as this is the component that transmits acoustic energy out of the domain:

$$\frac{\bar{\rho}\,\bar{c}\,\mathcal{P}_{nm}(M)}{R^2|P^+_{nm}|^2}=\pi J_{n+1}(\alpha_{nm})^2\frac{(1-M^2)^2\sqrt{1-(\alpha_{nm}/kR)^2(1-M^2)}}{[1-M\sqrt{1-(\alpha_{nm}/kR)^2(1-M^2)}]^2}$$

Forming the ratio $\mathcal{P}_{nm}(M)/\mathcal{P}_{nm}(0)$ eliminates the remaining nondimensional scaling factor and allows for easier interpretation:

$$\frac{\mathcal{P}_{nm}(M)}{\mathcal{P}_{nm}(0)}=\frac{(1-M^2)^2\sqrt{1-(\alpha_{nm}/kR)^2(1-M^2)}}{\sqrt{1-(\alpha_{nm}/kR)^2}[1-M\sqrt{1-(\alpha_{nm}/kR)^2(1-M^2)}]^2}\tag{23}$$

which shows a monotonic increase in downstream energy transmission with increasing Mach number.

Because of the nonuniform cross section of the RD-170 main chamber and the coupling effects with upstream components, this calculation cannot be taken as exact. As the flow traverses the chamber, the decrease in area causes acceleration that

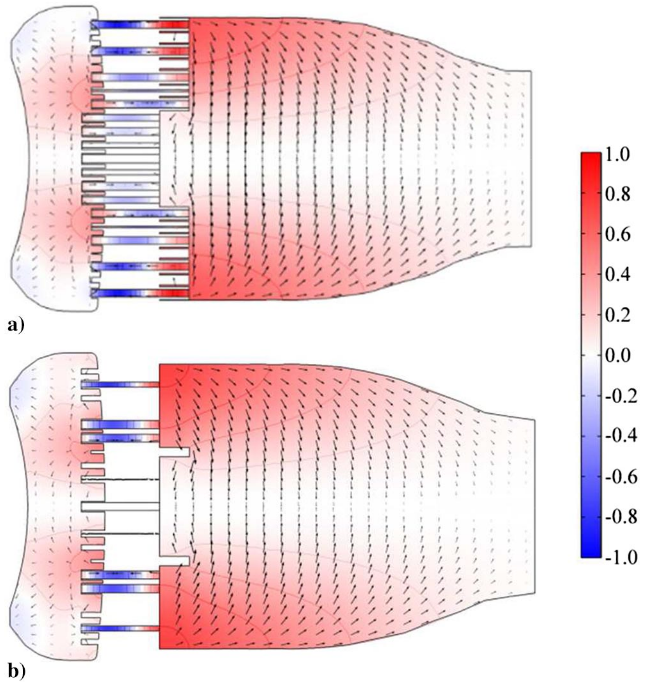

Fig. 20 Second tangential (2T) mode shapes of acoustic pressure and velocity 0° longitudinal cross section a) with and b) without injector damping.

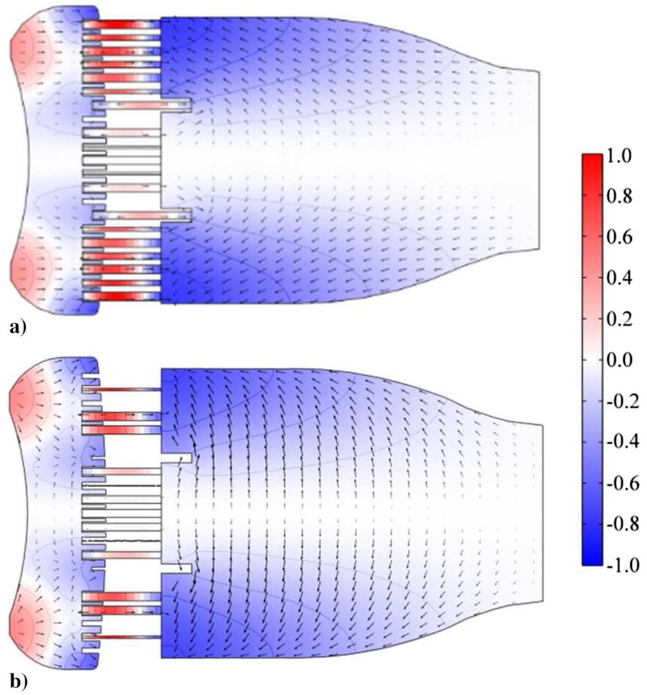

Fig. 21 Second tangential (2T) mode shapes of pressure and velocity 90° longitudinal cross section a) with and b) without injector damping.

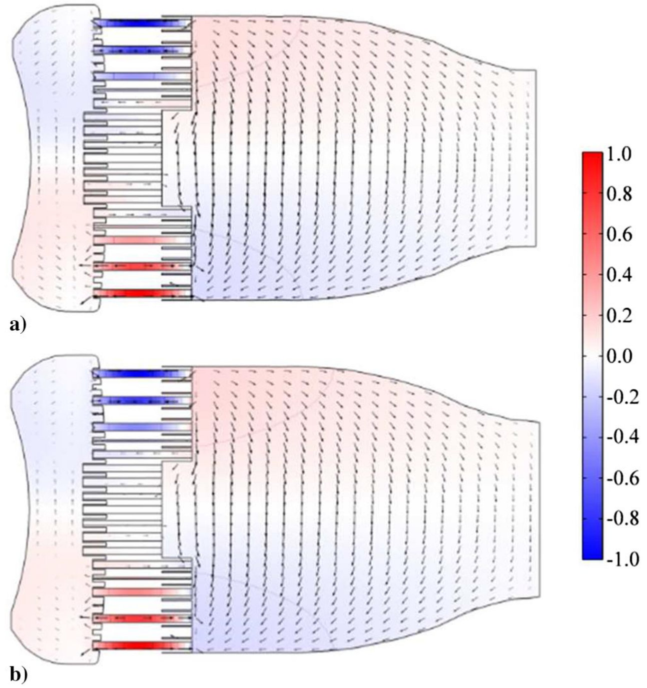

Fig. 22 First tangential (1T) mode shapes of pressure and velocity 0° longitudinal cross section a) with and b) without mean flow.

culminates at the throat. Furthermore, additional effects may arise due to acoustic refraction in regions with mean flow gradients. The present work, however, does provide some theoretical explanation for the increased damping due to mean flow, and particularly the increase in damping of the 2T mode over the 1T mode.

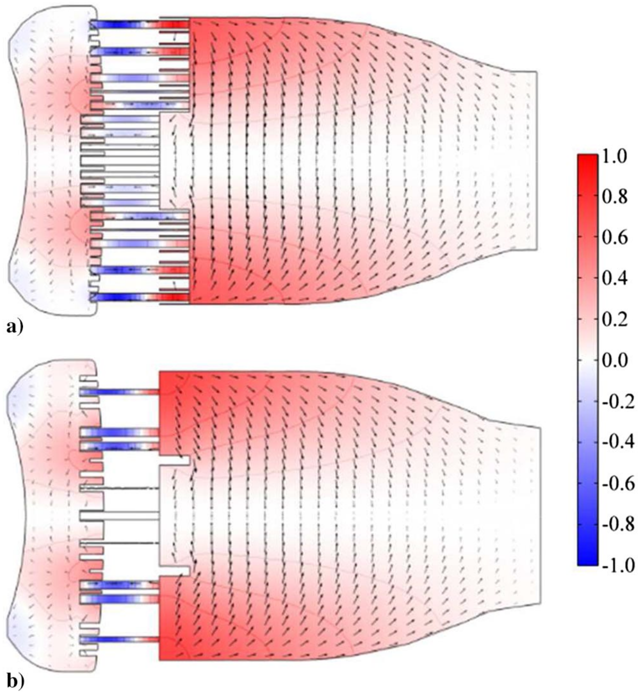

Fig. 23 Second tangential (2T) mode shapes of acoustic pressure and velocity 0° longitudinal cross section a) with and b) without mean flow.

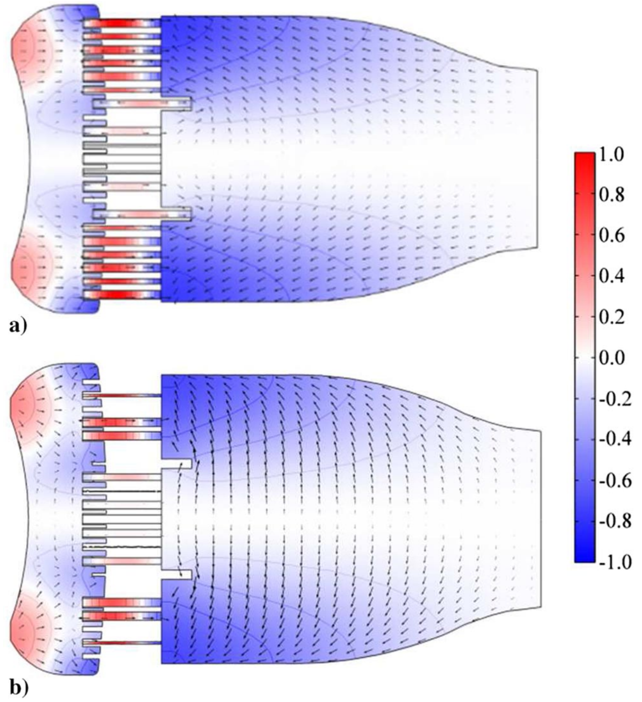

Fig. 24 Second tangential (2T) mode shapes of acoustic pressure and velocity 90° longitudinal cross section a) with and b) without mean flow.

Table 9 Effect of flow distributor impedance on frequency and damping coefficient

Mode	Mode frequency, Hz	Damped frequency, Hz
1T	1880	$1874 + 32.4i$
2T	3150	$3142 + 53.5i$

IV. Conclusions

A linear acoustic analysis has been developed and applied to the main combustion chamber of an ORSC engine. The work allows for the treatment of geometric details and mean flow effects. As a specific example, a combustion chamber similar to that of the RD-170 engine was considered, including the upstream oxidizer plenum, flow distributor, and injector assembly. This represents the most complex realistic geometric configuration considered in such an acoustic study to the authors' knowledge. A theoretical model for acoustic impedance based on unsteady vortex shedding at flow orifice rims was specified as a boundary condition at the flow distributor plate. An impedance model was also derived for viscous damping of acoustic waves within the injector assembly and incorporated into the model. Results for the acoustic field indicate that communication between the main chamber and oxidizer plenum affected by the injectors is significant. Acoustic waves excited in the main chamber propagate upstream through the injectors and interact with the oxidizer dome, where they are damped by the flow distributor. The largest contributor to damping is found to be mean flow. The phenomenon can be attributed to the increased downstream acoustic energy transmission.

Acknowledgments

This work was sponsored partly by the NASA Marshall Space Flight Center under Contract No. NNM12AA41C and partly by the William R. T. Oakes Endowment of the Georgia Institute of Technology.

References

[1] Lieuwen, T. C., and Yang, V., *Combustion Instabilities in Gas Turbine Engines: Operational Experience, Fundamental Mechanisms and Modeling*, Vol. 210, Progress in Astronautics and Aeronautics, AIAA, Reston, VA, 2005.

[2] Yang, V., and Culick, F. E. C., "Analysis of Low Frequency Combustion Instabilities in a Laboratory Ramjet Combustor," *Combustion Science and Technology*, Vol. 45, No. 1, 1986, pp. 1–25. doi:10.1080/00102208608923839

[3] Choi, J.-Y., Ma, F., and Yang, V., "Combustion Oscillations in a Scramjet Engine Combustor with Transverse Fuel Injection," *Proceedings of the Combustion Institute*, Vol. 30, No. 2, 2005, pp. 2851–2858. doi:10.1016/j.proci.2004.08.250

[4] Lin, K.-C., Jackson, K., Behdadnia, R., Jackson, T. A., Ma, F., and Yang, V., "Acoustic Characterization of an Ethylene-Fueled Scramjet Combustor with a Cavity Flameholder," *Journal of Propulsion and Power*, Vol. 26, No. 6, 2010, pp. 1161–1170. doi:10.2514/1.43338

[5] Sung, H.-G., and Yang, V., "Unified Analysis of Internal Flowfield in an Integrated Rocket Ramjet Engine. II: Ramjet Sustainer," *Journal of Aerospace Engineering*, Vol. 27, No. 2, 2012, pp. 398–403. doi:10.1061/(ASCE)AS.1943-5525.0000256

[6] De Luca, L., Price, E. W., and Summerfield, M., *Nonsteady Burning and Combustion Stability of Solid Propellants*, Vol. 143, Progress in Astronautics and Aeronautics, AIAA, Washington, D.C., 1992.

[7] Yang, V., Brill, T. B., and Ren, W., *Solid Propellant Chemistry Combustion and Motor Interior Ballistics*, Vol. 185, Progress in Astronautics and Aeronautics, AIAA, Reston, VA, 2000.

[8] Anderson, W. E., and Yang, V., *Liquid Rocket Engine Combustion Instability*, Vol. 169, Progress in Astronautics and Aeronautics, University Park, Pennsylvania, AIAA, Washington, D.C., 1995.

[9] Dranovsky, M. L., Yang, V., Culick, F. E. C., and Talley, D. G., *Combustion Instabilities in Liquid Rocket Engines: Testing and Development Practices in Russia*, Vol. 221, Progress in Astronautics and Aeronautics, AIAA, Reston, VA, 2007.

[10] Yang, V., Ku, D. D., Walker, M. L. R., Williams, L., and Leahy, J. C., "Liquid Oxygen/Kerosene Staged Combustion Rocket Engines with Oxidizer-Rich Preburners," NASA TP-2015-218203, 2015.

[11] Manski, D., Goertz, C., Saßnick, H.-D., Hulka, J. R., Goracke, B. D., and Levack, J. H., "Cycles for Earth-to-Orbit Propulsion," *Journal of Propulsion and Power*, Vol. 14, No. 5, 1998, pp. 588–604. doi:10.2514/2.5351

[12] Katorgin, B. I., and Chelkis, F. J., "The RD-170, A Different Approach to Launch Vehicle Propulsion," *AIAA/SAE/ASME/ASEE 29th Joint Propulsion Conference and Exhibit*, AIAA Paper 1993-2415, 1993. doi:10.2514/6.1993-2415

[13] Katorgin, B. I., Chvanon, V. K., Chelkis, F. J., Lozino-Lozinskaya, I. G., and Tanner, L. G., "Oxidizer-Rich Staged Combustion Rocket Engines Use and Development in Russia," *AIAA Space Programs and Technologies Conference*, AIAA Paper 1995-3607, 1995. doi:10.2514/6.1995-3607

[14] Culick, F. E. C., "A Note on Rayleigh's Criterion," *Combustion Science and Technology*, Vol. 56, Nos. 4–6, 1987, pp. 159–166. doi:10.1080/00102208708947087

[15] Yang, V., Kim, S. I., and Culick, F. E. C., "Triggering of Longitudinal Pressure Oscillations in Combustion Chambers. I: Nonlinear Gasdynamics," *Combustion Science and Technology*, Vol. 72, Nos. 4–6, 1990, pp. 183–214. doi:10.1080/00102209008951647

[16] Wicker, J. M., Greene, W. D., Kim, S.-I., and Yang, V., "Triggering of Longitudinal Combustion Instabilities in Rocket Motors—Nonlinear Combustion Response," *Journal of Propulsion and Power*, Vol. 12, No. 6, 1996, pp. 1148–1158. doi:10.2514/3.24155

[17] Balasubramanian, K., and Sujith, R. I., "Thermoacoustic Instability in a Rijke Tube: Non-Normality and Nonlinearity," *Physics of Fluids*, Vol. 20, No. 4, 2008, Paper 044103. doi:10.1063/1.2895634

[18] Juniper, M. P., "Triggering in the Horizontal Rijke Tube: Non-Normality, Transient Growth and Bypass Transition," *Journal of Fluid Mechanics*, Vol. 667, Jan. 2011, pp. 272–308. doi:10.1017/S0022112010004453

[19] Culick, F. E. C., "Nonlinear Behavior of Acoustic Waves in Combustion Chambers—I," *Acta Astronautica*, Vol. 3, No. 9, 1976, pp. 715–734. doi:10.1016/0094-5765(76)90107-7

[20] Flandro, G. A., Fischbach, S. R., and Majdalani, J., "Nonlinear Rocket Motor Stability Prediction: Limit Amplitude, Triggering, and Mean Pressure Shift," *Physics of Fluids*, Vol. 19, No. 9, 2007, Paper 094101. doi:10.1063/1.2746042

[21] Crocco, L., and Cheng, S.-I., *Theory of Combustion Instability in Liquid Propellant Rocket Motors*, Butterworths Scientific Publ., Princeton, NJ, 1956, Paper AD688924.

[22] Harrje, D., and Reardon, F., "Liquid Propellant Rocket Combustion Instability," NASA SP-194, 1972.

[23] Zinn, B. T., and Powell, E. A., "Nonlinear Combustion Instability in Liquid-Propellant Rocket Engines," Vol. 13, 1971.

[24] Culick, F. E. C., and Yang, V., "Prediction of the Stability of Unsteady Motions in Solid-Propellant Rocket Motors," *Nonsteady Burning and Combustion Stability of Solid Propellants*, Vol. 143, edited by L. De Luca, E. W. Price, and M. Summerfield, AIAA, Washington, D.C., 1992, pp. 719–779.

[25] Culick, F. E. C., and Yang, V., "Overview of Combustion Instabilities in Liquid-Propellant Rocket Engines," *Liquid Rocket Engine Combustion Instability*, Vol. 169, edited by W. E. Anderson, and V. Yang, 1995, pp. 3–37.

[26] Tamanampudi, G. M. R., and Anderson, W. E., "Development of Combustion Instability Analysis Tool by Incorporating Combustion Response Models," *51st AIAA/SAE/ASEE Joint Propulsion Conference*, AIAA Paper 2015-4165, 2015. doi:10.2514/6.2015-4165

[27] Pieringer, J., Sattelmayer, T., and Fassl, F., "Simulation of Combustion Instabilities in Liquid Rocket Engines with Acoustic Perturbation Equations," *Journal of Propulsion and Power*, Vol. 25, No. 5, 2009, pp. 1020–1031. doi:10.2514/1.38782

[28] Martin, C. E., Benoit, L. J.-L., Sommerer, Y., Nicoud, F., and Poinsot, T., "Large-Eddy Simulation and Acoustic Analysis of a Swirled Staged Turbulent Combustor," *AIAA Journal*, Vol. 44, No. 4, 2006, pp. 741–750. doi:10.2514/1.14689

[29] Searby, G., Habiballah, M., Nicole, A., and Laroche, E., "Prediction of the Efficiency of Acoustic Damping Cavities," *Journal of Propulsion and Power*, Vol. 24, No. 3, 2008, pp. 516–523. doi:10.2514/1.32325

[30] Kim, S.-K., Choi, H. S., Kim, H. J., Ko, Y. S., and Sohn, C. H., "Finite Element Analysis for Acoustic Characteristics of Combustion Stabilization Devices," *Aerospace Science and Technology*, Vol. 42, April–May 2015, pp. 229–240. doi:10.1016/j.ast.2015.01.024

[31] Schulze, M., and Sattelmayer, T., "Low-Order Modelling of the Non-Local Acoustic Reacting Combustion Chamber-Dome Interface in Rocket Engines," *19th AIAA International Space Planes and Hypersonic Systems and Technologies Conference*, AIAA Paper 2014-3086, 2014. doi:10.2514/6.2014-3086

[32] Wicker, J. M., Yoon, M. W., and Yang, V., "Linear and Non-linear Pressure Oscillations in Baffled Combustion Chambers," *Journal of Sound and Vibration*, Vol. 184, No. 1, 1995, pp. 141–171. doi:10.1006/jsvi.1995.0309

[33] Quinlan, J. M., Kirkpatrick, A. T., Milano, D., Mitchell, C. E., and Hinerman, T. D., "Analytical and Numerical Development of a Baffled Liquid Rocket Combustion Stability Code," *Journal of Propulsion and Power*, Vol. 28, No. 1, 2012, pp. 122–131. doi:10.2514/1.B34276

[34] You, D., Ku, D. D., and Yang, V., "Acoustic Waves in Baffled Combustion Chamber with Radial and Circumferential Blades," *Journal of Propulsion and Power*, Vol. 29, No. 6, 2013, pp. 1453–1467. doi:10.2514/1.B34923

[35] Howe, M. S., "On the Theory of Unsteady High Reynolds Number Flow Through a Circular Aperture," *Proceedings of the Royal Society of London A: Mathematical, Physical and Engineering Sciences*, Vol. 366, No. 1725, 1979, pp. 205–223. doi:10.1098/rspa.1979.0048

[36] Howe, M. S., *Acoustics of Fluid-Structure Interactions*, Cambridge Univ. Press, Cambridge, England, U.K., 1998, pp. 364–365.

[37] Luong, T., Howe, M. S., and McGowan, R. S., "On the Rayleigh Conductivity of a Bias-Flow Aperture," *Journal of Fluids and Structures*, Vol. 21, No. 8, 2005, pp. 769–778. doi:10.1016/j.jfluidstructs.2005.09.010

[38] Batchelor, G. K., *An Introduction to Fluid Dynamics*, Cambridge Univ. Press, New York, 1967, Chap. 6.

[39] Pierce, A. D., *Acoustics: An Introduction to Its Physical Principles and Applications, 20*, McGraw–Hill, New York, 1981.

[40] Lympany, S., and Ahuja, K. K., "Sound Damping by Injector Tubes and Surrounding Ducting used in Liquid Rocket Combustors," AIAA Paper 2016-3036, 2016.

[41] Culick, F. E. C., "Stability of Three-Dimensional Motions in a Combustion Chamber," *Combustion Science and Technology*, Vol. 10, Nos. 3–4, 1975, pp. 109–124. doi:10.1080/00102207508946663

[42] Myers, M. K., "On the Acoustic Boundary Condition in the Presence of Flow," *Journal of Sound and Vibration*, Vol. 71, No. 3, 1980, pp. 429–434. doi:10.1016/0022-460X(80)90424-1

[43] Wang, T.-S., "Thermophysics Characterization of Kerosene Combustion," *Journal of Thermophysics and Heat Transfer*, Vol. 15, No. 2, 2001, pp. 140–147. doi:10.2514/2.6602

[44] Svehla, R. A., and McBride, B. J., "FORTRAN IV Computer Program for Calculation of Thermodynamic and Transport Properties of Complex Chemical Systems," NASA TN D-7056, 1973.

[45] Bell, W. A., and Zinn, B. T., "The Prediction of Three-Dimensional Liquid-Propellant Rocket Nozzle Admittance," NASA CR-121129, 1973.

[46] Zinn, B. T., Powell, E. A., and Padmanabhan, M. S., "Determination of the Effects of Nozzle Nonlinearities Upon Nonlinear Stability of Liquid Propellant Rocket Motors," CR-139634, 1974.

[47] Jing, X., and Sun, X., "Effect of Plate Thickness on Impedance of Perforated Plates with Bias Flow," *AIAA Journal*, Vol. 38, No. 9, 2000, pp. 1573–1578. doi:10.2514/2.1139

[48] Flandro, G. A., Cai, W., and Yang, V., "Turbulent Transport in Rocket Motor Unsteady Flowfield," *Solid Propellant Chemistry, Combustion, and Motor Interior Ballistics*, Progress in Astronautics and Aeronautics, Vol. 185, AIAA, Reston, VA, 2000, pp. 837–858.

[49] Apte, S., and Yang, V., "Unsteady Flow Evolution in Porous Chamber with Surface Mass Injection, Part 2: Acoustic Excitation," *AIAA Journal*, Vol. 40, No. 2, 2002, pp. 244–253. doi:10.2514/2.1666

[50] Munjal, M. L., *Acoustics of Ducts and Mufflers with Application to Exhaust and Ventilation System Design*, Wiley, 1987.

[51] Dowling, A. P., and Stow, S. R., "Acoustic Analysis of Gas Turbine Combustors," *Journal of Propulsion and Power*, Vol. 19, No. 5, 2003, pp. 751–764. doi:10.2514/2.6192

F. Liu
Associate Editor

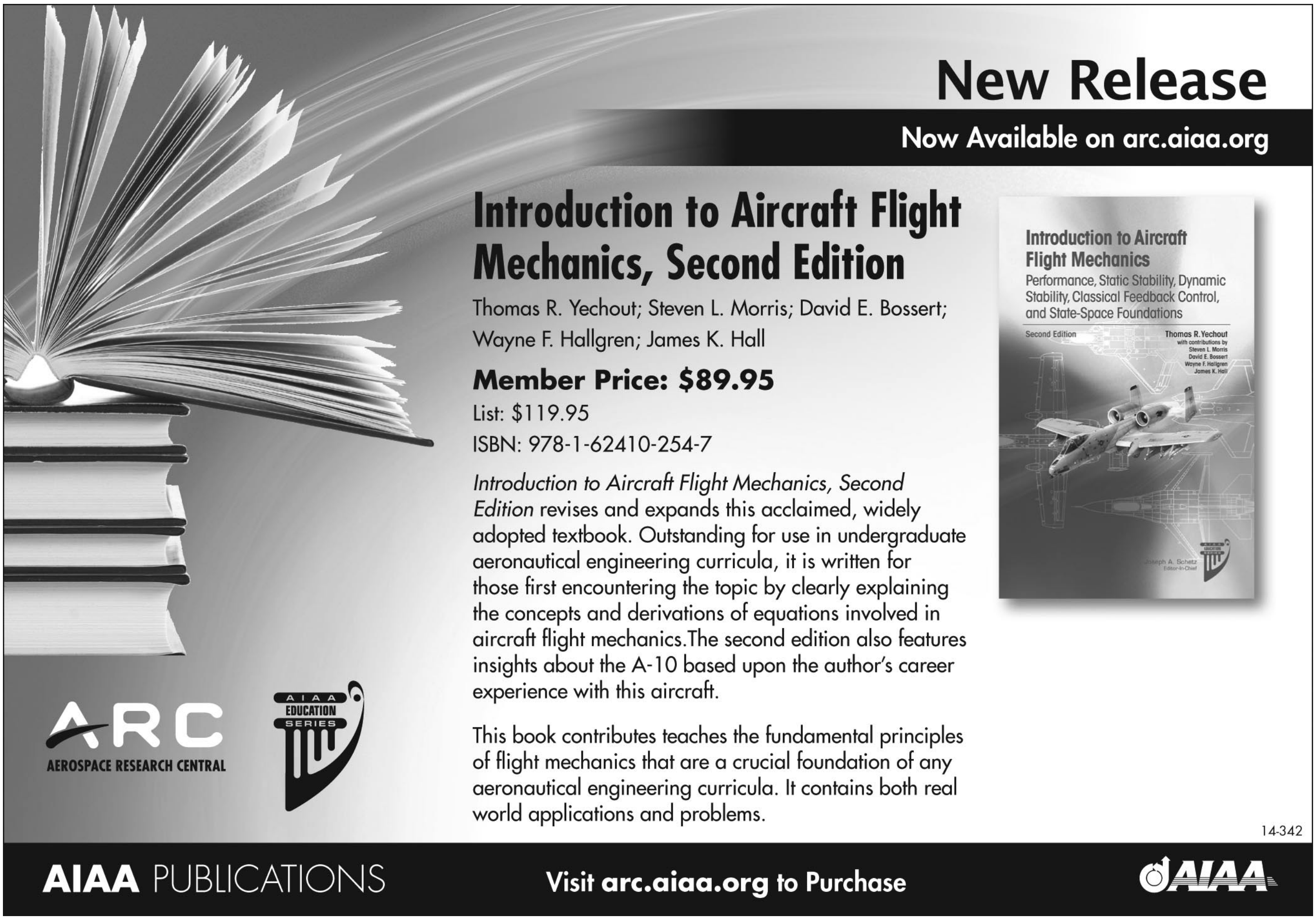

New Release

Now Available on arc.aiaa.org

Introduction to Aircraft Flight Mechanics, Second Edition

Thomas R. Yechout; Steven L. Morris; David E. Bossert; Wayne F. Hallgren; James K. Hall

Member Price: $89.95
List: $119.95
ISBN: 978-1-62410-254-7

Introduction to Aircraft Flight Mechanics, Second Edition revises and expands this acclaimed, widely adopted textbook. Outstanding for use in undergraduate aeronautical engineering curricula, it is written for those first encountering the topic by clearly explaining the concepts and derivations of equations involved in aircraft flight mechanics.The second edition also features insights about the A-10 based upon the author's career experience with this aircraft.

This book contributes teaches the fundamental principles of flight mechanics that are a crucial foundation of any aeronautical engineering curricula. It contains both real world applications and problems.

ARC AEROSPACE RESEARCH CENTRAL

AIAA EDUCATION SERIES

14-342

AIAA PUBLICATIONS Visit arc.aiaa.org to Purchase AIAA